ORIGINAL ARTICLES

CrossMark

Manufacturing and Characterization of a Carbon-Based Amorphous (a-CN$_X$) Coating Material

Md.Masud-Ur Rashid[1] · Andreas Archenti[1]

Abstract

A thick 400-micron amorphous carbon nitride (a-CN$_X$) coating material was synthesized by means of plasma-enhanced chemical vapor deposition process. High-power impulse magnetron sputtering technique was used to sputter a pure graphite target plate in reactive argon (Ar), nitrogen (N$_2$) and acetylene (C$_2$H$_2$) environment for depositing the composite coating. Structural and chemical/elemental composition of the a-CN$_X$ composite material was investigated by field emission scanning electron microscopy, energy-dispersive X-ray spectroscopy and micro-Raman spectroscopy. The root-mean-square surface roughness (S_q) and structure were estimated by atomic force microscopy. Mechanical properties such as hardness and Young's modulus (Oliver–Pharr method) at room temperature were characterized by Vickers micro-indentation test. Operational temperature test of the deposited a-CN$_X$ coating reveals that it can withstand up to 400 °C without cracking. An inverted shaker test, based on central impedance method, was adopted to investigate the dynamic damping property of the coating material, and it was found that the first bending mode damping lossfactor of the reported a-CN$_X$ coating is 0.015 ± 0.001 and corresponding loss modulus (Young's modulus multiplied by lossfactor) is 0.234 ± 0.011 GPa.

Keywords PECVD · Reactive HiPIMS · Amorphous carbon nitride (a-CN$_x$) · Mechanical properties · Material properties · System damping lossfactor · Material damping lossfactor

1 Introduction

Carbon, with its different forms and alloys, has significant importance in our modern life due to the fact that graphite can be used in various mechanical applications, and because amorphous carbon films can be used as protective layer in computer hard disk [1]. Carbon-based thin (< 1 μm) or thick (> 1 μm) films were developed to address a broad range of functional applications such as hydrogen-free amorphous carbon nitride (a-CN$_X$) film is used as direct current (DC) electrical conductor to increase

electrical conductivity [2], as wear resistance against non-lubricated surfaces due to its excellent low friction coefficient [3], as hard protective layers in magnetic storage devices [4], and in biomedical applications for reducing orthodontic friction between archwire and bracket both in ambient air and saliva [5]. Several studies demonstrated that carbon-based amorphous films have lower internal stress and good adhesion [6], high load bearing capability [7], high sliding wear resistance [8], low friction coefficient [9], and excellent elastic recovery and hardness [10].

While most of the research works of carbon nitride films have been focused on studying the mechanical properties such as the hardness, the resilient or elastic recovery behavior and the elastic modulus, very few research works [11–13] have been carried out focusing on mechanical vibration damping capacity of thick (> 100 μm) amorphous carbon nitride coating. Fu et al. demonstrated that copper (Cu) inclusion in amorphous carbon nitride matrix can significantly suppress self-excited vibrations such as chatter during turning [11] and milling [12] operations, as

✉ Md.Masud-Ur Rashid
   mmuras@kth.se

   Andreas Archenti
   archenti@kth.se

1 Department of Production Engineering, Manufacturing and Metrology Systems Division, Precision Engineering and Metrology, KTH Royal Institute of Technology, Brinellvägen 68, 10044 Stockholm, Sweden

well as the copper inclusion can substantially increase dynamic stiffness of the cutting tool during the milling operation [13].

In this work, a thick 400 μm amorphous carbon nitride (a-CN_X) coating, first introduced in [13], is synthesized successfully by high-power impulse magnetron sputtering (HiPIMS) of pure graphite target plate in reactive Ar/N_2/C_2H_2 environment, and the coating material's microstructure and mechanical properties including the mechanical vibration damping capacity are fully investigated. Discharge current–voltage waveform of the experimentally used HiPIMS process is thoroughly explained to understand the observed properties of the synthesized a-CN_X coating.

1.1 State of the Art of a-CN_X Material

The microstructure of a-CN_X films such as 'graphite-like carbon nitride' and 'fullerene-like carbon nitride' depends on the incorporating ratio of sp^3 and sp^2 hybridized bonding between carbon and nitrogen [14]. Mechanical properties such as hardness and Young's modulus of a-CN_X films increase with increasing sp^3 hybridized bonds [15]. Bakoglidis et al. [16] deposited a series of a-CN_X thin films using medium frequency magnetron sputtering (MFMS), high-power impulse magnetron sputtering (HiPIMS) and direct current magnetron sputtering (dcMS) techniques. In all three cases, they used almost same process parameters and compared the mechanical properties of the deposited films. They found that the film produced by MFMS has the highest hardness (24.6 GPa) and elastic recovery value (90.7%) as well as the film has the highest compressive stress (4.2 GPa), while the film deposited by HiPIMS has the moderate amount of hardness value (14 GPa) and the lowest compressive stress (1.2 GPa). They argued that the high elasticity of the films is originated by sp^2 hybridized bonds which increases with increasing substrate bias voltage.

The mechanical and tribological properties of carbon-based coatings can be tailored by controlling the energy and flux of the depositing ions, radicals and molecules to substrates [17, 18] in various high plasma density discharge-based deposition processes such as cathodic vacuum arc (CVA) [19], pulsed laser deposition (PLD) [20], inductively coupled plasma (ICP) [21], plasma-enhanced chemical vapor deposition (PECVD) coupled with electron cyclotron resonance [22], and magnetron sputtering [23]. Comparing to direct current magnetron sputtering (dcMS) and radio frequency magnetron sputtering (RFMS), high-power impulse magnetron sputtering (HiPIMS) process is known to generate higher plasma density (10^{19} m^{-3} comparing to 10^{17} m^{-3} in dcMS) [24, 25]. This high plasma density in HiPIMS is beneficial not only for creating the highly ionized carbon particles in case of sputtering the graphite target plate but also for increasing the depositing ion flux [25] which eventually create superior mechanical properties in a-CN_X coating [26].

Thick a-CN_X film deposition on steel substrate by magnetron sputtering process is limited due to poor adhesion between the film and substrate as well as because of high compressive stress which can be built up inside the film during the deposition process [27]. Wang et al. [28] reported that after a certain critical bias voltage (− 150 V), the adhesion between the film and substrate decreases with increasing bias voltage. They argued that adhesion depends on internal stress of the film which increases with increasing bias voltage, and they also pointed out that lower sp^3 hybridized carbon bonds, pulse bias voltage and oxygen contents in the films are responsible for lower internal stress which eventually increase the adhesion between the graphite-like carbon (GLC) film and substrate. Wang et al. [29] demonstrated that during GLC amorphous films deposition by unbalanced magnetron sputtering process hardness and internal stress of the film increase with increasing duty cycle. Huang et al. [30] reported that the internal stress of the graphite-like carbon films increases with increasing HiPIMS cathode voltage. In their case, the highest internal stress value was found to be 2.5 GPa at the − 1000 V of HiPIMS cathode voltage. Liao et al. [31] discovered that by forming a gradient interlayer at the interface, adhesion between the substrate and film could be improved. One possible solution to increase the adhesion is to activate the substrate surface by plasma etching pretreatment prior to the deposition process. Another practice is to apply some kind of additive layer by means of sputtering the metal target material between the film and substrate as a bonding agent. Broitman et al. [27] demonstrated that the high energy chromium (Cr) plasma etching in HiPIMS can substantially clean the oxide and other contaminants from the steel substrate surface and thus can enhance the adhesion. They also showed that a thin sublayer of Cr (100 nm) as well as amorphous transition layer deposited by HiPIMS in master–slave configuration can further increase the adhesion. Broitman et al. [32] reported that the stress in amorphous carbon nitride film is a function of the deposition temperature. Up to a certain temperature level (350 °C), the compressive internal stress increases with increasing temperature as well as the microstructure changes from amorphous to dense graphitic, but after 350 °C, up to 600 °C stress decreases with increasing temperature. They also demonstrated that the internal stress of the film decreases with increasing partial pressure of nitrogen (N_2). At the low growth temperature, the microstructure of the carbon nitride film, deposited in reactive magnetron sputtering of graphite in Ar/N_2 discharge, evolves from amorphous to columnar amorphous structure [32].

Reactive hydrocarbon gas inclusion in magnetron sputtering of graphite target discharge is known to increase deposition rate, though it has the disadvantage of generating hydrogen (H)-based species in bulk plasma which are detrimental to the desired mechanical properties of the deposited films [33]. Nonetheless, Aijaz et al. [23] demonstrated that hydrogenated amorphous carbon thin film can be synthesized with low hydrogen quantity in Ar/C_2H_2 discharge. They argued that the high plasma density of superimposed HiPIMS and dcMS facilitates to reduce the hydrogen quantity in the deposited film through chemical sputtering of growing film surface, and thereby hardness and mass density of the film are increased.

2 Experimental Details

2.1 Synthesis of Amorphous Carbon Nitride (a-CN$_X$) Coating Material

2.1.1 Experimental Setup

A novel plasma-enhanced chemical vapor deposition (PECVD) process equipped with single magnetron cathode was used for the deposition of 400 μm thick a-CN$_X$ coating material. The single magnetron cathode was driven by high-power impulse power scheme. The PECVD reactor used for this work consists of a rectangular stainless steel deposition chamber (length × width × height = 1.33 m × 0.30 m × 0.30 m) placed inside of a cylindrical vacuum chamber (length 2.00 m and diameter 1.00 m) which is also made of stainless steel, as seen in Fig. 1a.

The whole vacuum chamber was pumped down by a Pfeiffer vacuum system, combination of a rotary vane pump (Model: DUO 065D) and a turbo molecular pump (model: TC750), to the background pressure of equal to or less than 0.001 Pa. A graphite target plate (99.99% pure), placed from the top of the rectangular deposition chamber, was sputtered in Ar/N_2/C_2H_2 reactive environment for the deposition of the a-CN$_X$ coating. For this purpose, a standard planar rectangular balanced magnetron with a surface area of 0.45 m × 0.1 m was mounted behind the target plate. The length and width of the target plate are 0.62 and 0.12 m, respectively, which give the surface area of 0.074 m^2. The mixture of neutral gas (Ar) and reactive precursor gases (N_2 and C_2H_2) was fed into the chamber through the cathode area opening in front of the target plate. The flow was controlled by a feed through valve. In the gas mixture, the ratio of the partial pressure (in *pascal*) of the neutral and precursor gases was kept constant at 1:1:1 (Ar/N_2/C_2H_2) and the total process pressure was adjusted between 2 and 3 Pa by a proportional valve during the entire deposition process. In deposition chamber setup,

the target plate to substrate distance can be varied by moving the cathode housing up and down, but in this work the position of the substrates was fixed to 0.1 m away from the target plate surface. The a-CN$_X$ coating deposition was carried out at ambient temperature without any intentional external heating. All substrates were mounted on a rotating fixture inside the vacuum chamber, and an AC motor was used for rotating substrate at 1.3 rpm. A schematic representation of the PECVD process used for the deposition of a-CN$_X$ material is shown in Fig. 1b.

2.1.2 HiPIMS Deposition Process

The HiPIMS deposition process used in this experiment is a class of plasma-based sputtering process such as PECVD [34] in which gas phase chemistry is activated by using the energy from plasma discharge rather than using external thermal energy [35]. In reactive HiPIMS so-called impulses (unipolar pulses) containing high power are applied to the magnetron target at low duty cycle (0.5–5%) and at low pulse frequency (50 Hz to 5 kHz) while keeping the average power less than 2 orders of magnitude of the peak discharge power [36]. This results in high peak power density of 0.1–1 kW/cm^2 to the target, which can generate a high plasma density in terms of highly ionized fraction of sputtered target material species and of used gaseous particles [37]. The high ionization fraction allows better control of the film growth by controlling the energy and direction of the depositing species [34]. Detail process parameters of this kind of HiPIMS process are given elsewhere [37]. In this work such a HiPIMS deposition system of having peak cathode voltage of − 1.1 kV was applied across the volume of neutral and reactive precursor gases between the cathode and anode (substrate and chamber wall). Pulses up to 100 A with pulse duration 400 μs and pulse repetition frequency of 330 Hz (which gives 66 kW peak power and 7.92 kW average power) were used by using an in-house developed power supply unit capable of delivering − 2000 V and 200 A peak cathode voltage and current rating, respectively. Details of this power scheme were described elsewhere [38]. This instantaneous high-power density to the cathode target plate generates a tremendous amount of charge carriers, which in terms of electron density is the order of 10^{18}–10^{19} m^{-3}, in the vicinity of target plate during the high-power impulse mode [37]. The high electron density in HiPIMS discharge facilitates to dissociate the C_2H_2 and N_2 precursor gases for creating ionized plasma which eventually lead to the formation of compound nitride coating on the substrates. With the main power supply, an automatic power switch was used as an arc-monitoring circuit which automatically cut off the power if it finds 100 continuous arcs per second. Target voltage and target current were
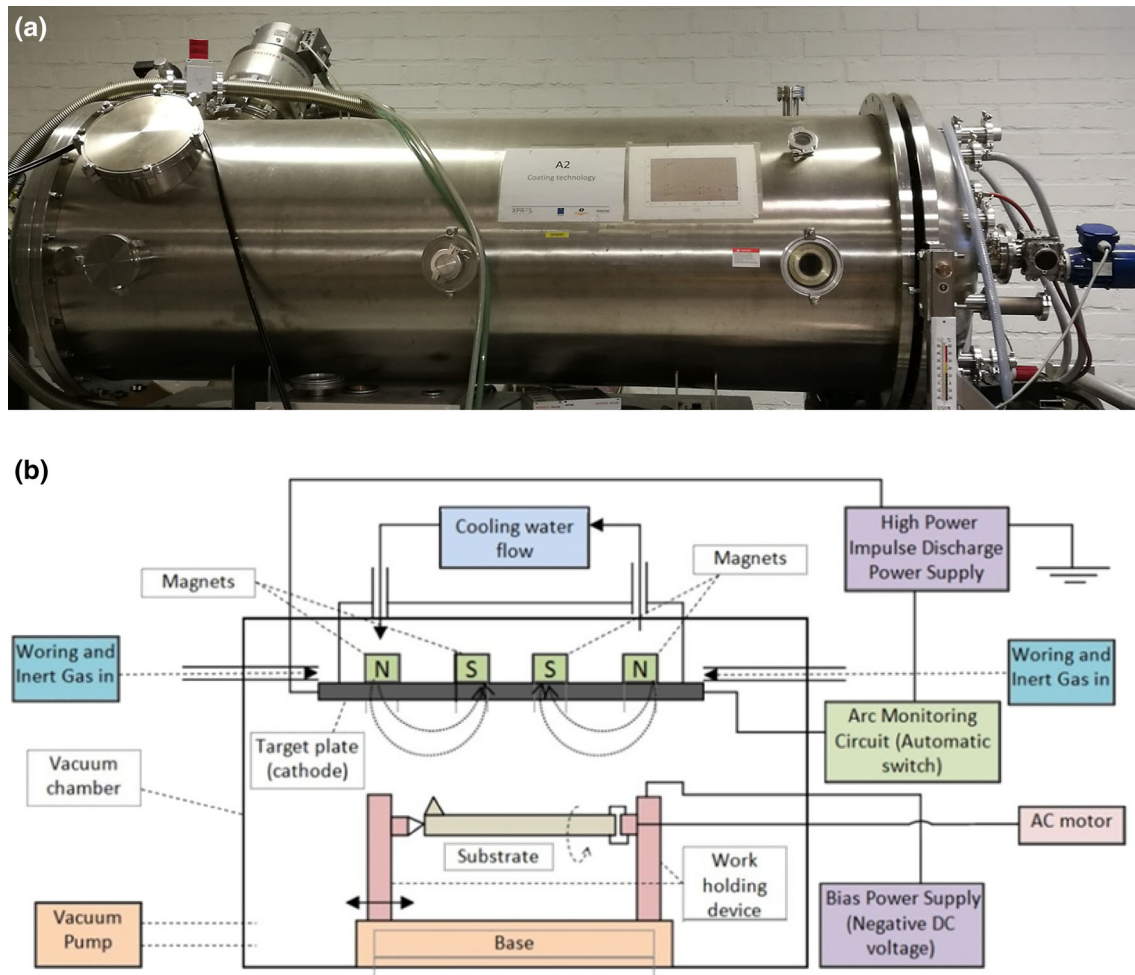
Fig. 1 **a** Cylindrical vacuum chamber, **b** schematic illustration of the PECVD process coupled with HiPIMS used in this work

measured as well as they were monitored by an Agilent DSO1004A oscilloscope. A Tektronix P6007 high-voltage probe and a Chauvin Arnoux C160 current probe measured the target voltage and current, respectively. Figure 2 shows the typical discharge current–voltage waveform of the high-power impulse magnetron sputtering of graphite target plate in $Ar/N_2/C_2H_2$ reactive PECVD process.

During carbon-based film deposition process, energetic ion bombardment of the substrate causes a very high intrinsic compressive stress into the film microstructure [39]. Again, due to the difference in temperature gradient of the steel substrate and carbon nitride film layer, thermal stress is induced at the interface [35]. These high compressive and thermal residual stresses tend to detach the film from the substrate after a critical film thickness. For this reason, prior to a-CN_X coating deposition process a relatively soft and ductile thin copper layer was deposited onto the substrate surface by high-power impulse magnetron sputtering of copper (Cu) target plate (99.9% in purity) in pure Ar gas environment at 0.83 Pa process

pressure. During this, thin Cu layer deposition process varying negative bias voltage was applied to the substrates for 80 min. Starting from − 350 V after each subsequent 10 min the bias voltage was reduced by 50 V, and thus in last 10 min the deposition was conducted without any bias voltage. This thin copper layer facilitates the substrate–coating layer interface sliding by acting as a metallurgical glue layer [27], and thus minimizes the effect of those compressive and thermal residual stresses. The DC bias voltage was used so that the neutral copper atoms and ions could be strongly implanted into the substrate surface, promoting the formation of an adherent interface between the substrate and the coating [27]. After Cu pre-layer deposition the copper target plate was replaced by the graphite target plate. The vacuum deposition chamber was further pumped down to the background pressure and argon plasma etching of pre-copper layer was conducted for 10 min to remove the contamination from the pre-copper layer surfaces. Argon, nitrogen and acetylene gas mixture in 1:1:1 partial pressure ratio was fed into the deposition

Fig. 2 Cathode Peak voltage and current waveform of HiPIMS of graphite target discharge in reactive Ar/N$_2$/C$_2$H$_2$ environment. Process pressure 2.5 Pa, pulse length 400 μs, pulse frequency 300 Hz
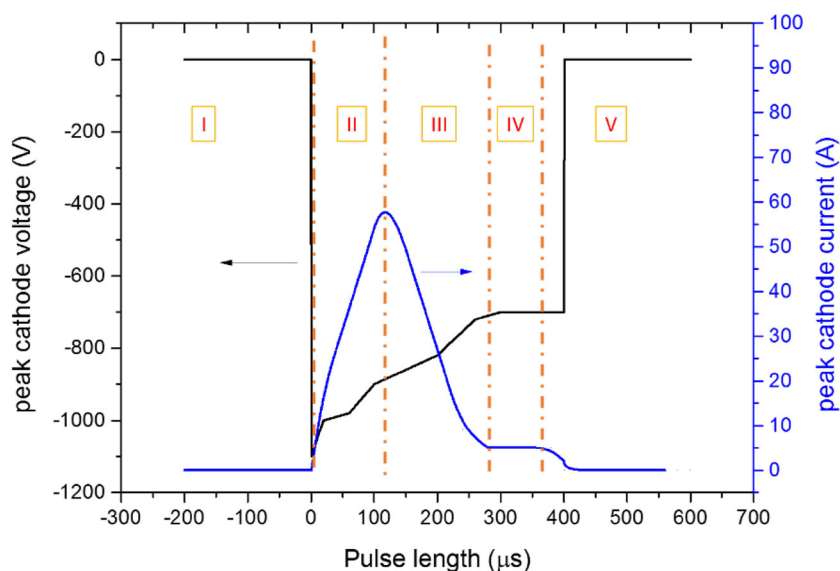
chamber, and the main carbon nitride deposition process was started. The first 80 min of the a-CN$_X$ deposition process was carried out at the same way of pre-copper layer deposition step with varying DC negative bias voltage for growing gradual interface layer of CN$_X$. The detail process parameters are listed in Table 1.

One steel bar (length 0.2 m, width 0.02 m, height 0.002 m) and five pure silicon (Si) pieces were used as substrates for the deposition of a-CN$_X$ coating material. Total deposition time for 400 μm thick coating layer was 49 h.

2.1.3 Substrates Cleaning and Pretreatment

Before loading into the deposition chamber, all the substrates were cleaned in following the stages of scrubbing with alkaline detergent, rinsing in distill water, ultrasonic bath cleaning with isopropanol and acetone for 30 min, and drying with hot air. For steel bar substrate, an extra step was followed to clean the substrate surface mechanically by abrasive grit (Glass bubble of 100–200 μm diameter in size) blasting and then followed the prior cleaning stages again. In situ plasma cleaning of the substrates was done in two steps. At first step, substrate surfaces were plasma etched by high energy positive argon ion (Ar$^+$) bombardment with the application of − 600 V, 100 kHz medium frequency bias voltage pulses to the substrate. This kind of medium frequency sputter cleaning with energetic gas ions is known to be very efficient for eliminating the oxide and other contaminants from the substrate surfaces [27]. Secondly, the substrate surfaces were plasma cleaned by positively charged carbon ions (C$^+$) and argon ions (Ar$^+$) in

Table 1 Parameters used for the deposition of 400 μm thick a-CN$_X$ coating material by the Reactive HiPIMS system

	In situ plasma cleaning	Pre-Cu layer deposition	Plasma etching of Pre-Cu layer	In situ plasma cleaning in HiPIMS mode	CN$_x$ coating material deposition process
Target plate	Copper	Copper	Graphite	Graphite	Graphite
Background pressure (Pa)	0.0065				
Ar gas flow rate (sccm)	117.55	117.55	117.55	331.16	186.45
N$_2$ gas flow rate (sccm)	–	–	–	–	55
C$_2$H$_2$ gas flow rate (sccm)	–	–	–	–	28.61
Peak discharge voltage (V)	–	900	–	1050	1100
Peak discharge current (A)	–	85	–	70	60
Pulse width (μs)	–	400	–	400	400
Pulse frequency (Hz)	–	300	–	300	300
Process pressure (Pa)	0.82	0.83	0.83	1.5	2.5
Bias voltage (V)	− 600	− 350 to 0	− 600	− 600	0
Process duration	10 min	1 h 20 min	10 min	35 min	47 h 31 min

HiPIMS mode. At this step − 600 V bias voltage with medium frequency (100 kHz) was also applied to the substrates. Graphite target plate was sputtered in pure Ar gas environment, and medium frequency negative bias voltage attracted the energetic (> 100 eV) positively charged sputtered carbon and argon ion fluxes to the substrate which eventually lead to the high energy ion bombardment of the substrate surfaces. This procedure not only clean the substrate, but also produce low-energy implantation of energetic ions, promoting the formation of a graded interface between the substrate and the coating which will increase the adhesion between the amorphous carbon nitride coating and substrates [27]. Detail process parameter of these steps is depicted in Table 1.

2.2 Material Characterization of the a-CN$_X$ Coating

Cross-sectional microstructure image of the deposited a-CN$_X$ coating material was acquired by using field emission scanning electron microscopy (FESEM, Zeiss Ultra Plus). For SEM micrographs, resin-embedded sample (a-CN$_X$ coating on Si substrate) was polished mechanically from coarser sandpapers to final polish with silica nanoparticles. The thickness of the deposited a-CN$_X$ coating was evaluated from the SEM cross-sectional micrograph An EDS analyzer equipped with FESEM was used to analyze the elemental composition of the coating. X-ray spectra were collected and quantified from 6 to 12 different positions from the coating cross section for identifying the chemical elements in the composite. Density of the a-CN$_X$ coating was calculated by dividing measured weight difference of the coated and uncoated steel bars by the coating volume. Weights of the uncoated and coated steel bars were measured by an automatic balance (sartorius, BP161P). Ten measurements were taken for each sample. Morphology and surface roughness of the a-CN$_X$ coating (on Si substrate) were evaluated by atomic force microscopy (AFM, Veeco Dimension 3100 SPM) operated in intermittent mode in air using conical Si tips with a typical tip radius of 10 nm and a length of ~ 20 μm (NSC14/AIBS MikroMash, Tallin, Estonia). AFM images were analyzed by using the SPIP 6.3.2 software (Image Metrology A/S, Hørsholm, Denmark). Root-mean-square (RMS) surface roughness value, S_q, was determined on 80×80 μm^2 area of the sample. Raman spectroscopy (Horiba Jobin–Yvon LabRAM HR800, Ar$^+$ laser source at $\lambda = 488$ nm) was used to evaluate the carbon structure of the coating. The Young's modulus and the hardness of the deposited a-CN$_X$ coating material were measured by Oliver and Pharr method [40] by using Vickers hardness microindenter (CSM Instruments, Switzerland, geometric factor GF = 2). Twelve indents were performed on the deposited

a-CN$_X$ coating (on Si substrate), and load–displacement curves were computed under linear loading condition with maximum applied load force of 5 N, rate of indention 15 μm/min, loading/unloading rate of 10 N/min and with 10 s holding time at the maximum indentation depth (h_{max}). For characterizing the operational temperature range of the deposited a-CN$_X$ coating, heating–cooling cycle was applied to the coated sample (a-CN$_X$ coated Si substrate) using a Linkam heating–cooling stage. Temperature was increased and decreased at 10 °C interval in the range of 30–450 °C. At each stage, an optical image was acquired after 60 s of the desired temperature level.

2.3 Mechanical Vibration Damping Lossfactor Calculation

The system damping lossfactor of the coated and uncoated steel bar was measured by central impedance method [41] at the room temperature, where the test piece was kept at free–free boundary condition. This method was adopted in so-called inverted shaker technique where a shaker (TIRA TV 50018) was kept free hanging in the air (suspended by the elastic wire attached to a rigid frame), and the sample was attached to the stinger of the shaker with an impedance head in between. The schematic view of the test setup is shown in Fig. 3. The impedance head (Dytran combined force and acceleration sensor, S/N 1303) used in this experiment, measures force and acceleration simultaneously at the center point of the sample.

Four levels of excitation force were applied to the test pieces with white noise excitation signal, and the corresponding 'accelerance' frequency response function (FRF) was measured to quantify the system damping lossfactor at each level of force. The stinger of the shaker was placed properly at the center point of the test piece to avoid excitation of torsional modes, and only first bending mode was excited. The natural frequencies of the uncoated and coated bar were obtained by the location of peaks of the corresponding FRF. However, due to the difficulties of identifying the response's amplitude in low damping uncoated and coated steel bar, the system lossfactor was evaluated based on the frequencies where the real part of the 'accelerance' frequency response function (FRF) crosses zero and nearby where it reaches to maximum and minimum points as shown in Fig. 4.

The mechanical contact between the different components in Fig. 3 could generate some damping due to the joint interfaces, and the contributions of these mechanical joints were higher than that of the material's damping of the substrate (steel bar). It was therefore necessary to take a certain number of measurements to get a statistical average of the mechanical system's lossfactor of the test piece. So, all the measurements were repeated four times.
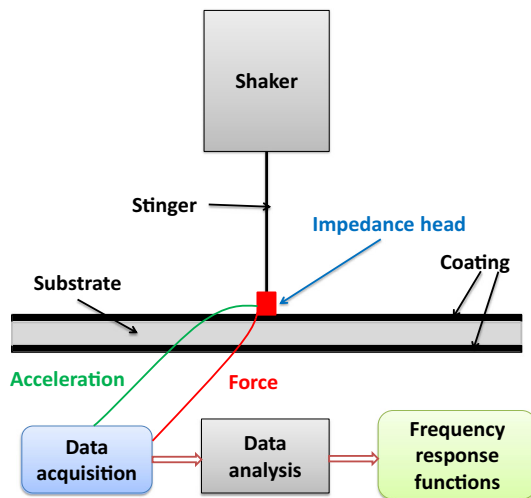
Fig. 3 Schematic experimental setup of the inverted shaker test

The system modal damping lossfactor was estimated according to Eq. (1) based on the theory of the low damping composite beam proposed in [42].

$$\eta_{\text{sys}} = \frac{f_2^2 - f_1^2}{f_2^2 + f_1^2} \qquad (1)$$

The modal material damping lossfactor of the coating material was estimated based on the theory of 'damping of free layer coating' presented in [43]. Since the material modal damping lossfactor of a-CN$_X$ coating is evaluated based on the ratio of the system modal damping lossfactor of the uncoated and coated bar as per Eq. (2), the measurement uncertainties due to external effects such as temperature, humidity, air damping and damping from exciting shaker can be neglected

$$\eta_{\text{sys}} = \frac{\eta_{\text{sub.}} E_{\text{sub.}} I_{\text{sub.}} + \eta_{\text{coat.}} E_{\text{coat.}} I_{\text{coat.}}}{E_{\text{sub.}} I_{\text{sub}} + E_{\text{coat.}} I_{\text{coat.}}} \qquad (2)$$
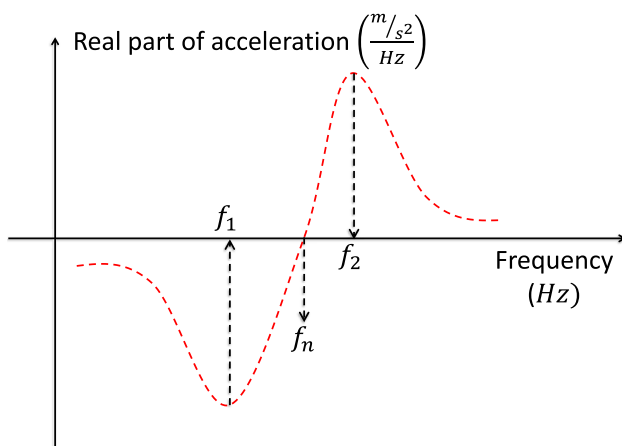

Fig. 4 Frequencies at where the 'accelerance' FRF reaches minimum (f_1), maximum (f_2) and crosses zero (f_n)

where E is Young's modulus, I is area moment of inertia, and η is lossfactor. The foot note 'sys.' indicates parameters for coating system (coated sample), foot note 'sub.' indicates parameters for substrate and foot note 'coat.' indicates parameters for coating material.

3 Results and Discussions

3.1 Discharge Current–Voltage Waveform Characteristics

The most convenient approach to understand the discharge characteristic of reactive/non-reactive sputtering process is to analyze the discharge current voltage waveform of that process [34]. The shape of discharge current waveform depends not only on the power supply used but also on the mode of operation. Reactive N_2 and C_2H_2 gases were mixed with neutral Ar gas in equal amount (33.33% in pressure percentage for all three gases) and fed into the deposition chamber. Within the process pressure of 2–3 Pa, average power was kept constant at 7.92 kW while peak cathode power was 66 kW. The peak cathode current density (considering the race track area of the target plate) and the duty cycle of the HiPIMS were 0.13 A/cm^2 and 12%, respectively. The reactive gases present in the system can form compound material onto the target surface (target surface poisoning) and depending on the degree of target surface poisoning shape and width of discharge pulse as well as peak amplitude of the discharge pulse can change significantly [34, 44]. HiPIMS discharge pulse shown in Fig. 2 can be divided into five different phases, during the 400 µs pulse width, such as 'ignition' (phase I), 'current rise' (phase II), 'gas rarefaction' (phase III), 'self-sputtering' (phase IV) and 'after glow' (phase V) [36, 44]. These different phases of discharge pulse also depend on target material, pulse frequency, magnetic field configuration, gas composition, and other plasma factors [45–47]. In general, the pulse discharge in Fig. 2 can be characterized by the sharp current rise to the peak value within approximately one-third of the pulse width followed by a drop within approximately two-third of the pulse width and then more or less a stable current plateau.

At the beginning of discharge, the peak cathode voltage is − 1100 V and 10–12 µs delay is observed before igniting the plasma (phase I). At this stage, negligible amount of plasma is present near target surface. Within this initial phase of 10–12 µs, glow discharge of metastable Ar gas atoms is about to be ignited near the target vicinity [48]. A short burst of hot electrons (70–100 eV) can be detected within this short time period indicating the start of electron impact excitation of Ar gas atoms and therefore Ar

gas temperature starts to increase at around 600–800 K due to the increased amount of collisions [48, 49].

After ignition phase, discharge current starts to rise and within 100 µs it reaches to peak value of 60 A. A drop of discharge voltage to approximately − 900 V is observed at the peak value of discharge current (phase II). At this stage, electrons created near the target region as well as secondary electrons are accelerated to the bulk plasma following the magnetic field lines. Neutral Ar gas starts to become ionized as well as ionization of sputtered vapor from target surface, dissociation of reactive N_2 and C_2H_2 gases begin [48]. However, this phase is dominated by neutral gas (Ar) ions [50].

At phase III (gas rarefaction), discharge current starts to decrease and reaches to minimum 5 A within approximately 200 µs. Discharge voltage also drops to approximately − 700 V. At this stage due to higher dissociation and ionization of precursor gases (N_2 and C_2H_2) comparing to constant gas flow rate, a strong reduction of precursor gas atom densities happens in target vicinity. At the same time due to high collisions between the sputtered carbon atoms and Ar gas atoms, heating and expansion of Ar gas take place. This phenomenon is known as gas rarefaction [34]. It can be speculated that comparing to the sputtering yield of graphite target plate sputtering yield of deposited compound material on graphite target is very low, which is also responsible for current drops during this phase. This can also be realized further by observing that the discharge current does not reach to second peak value after this phase which is common for Ar/O_2 reactive sputtering case [34].

In case of sufficient target power density, some portion of sputtered target material (graphite) ions can be back attracted to the target to further participate in the sputtering process and this is known as self-sputtering [34]. At this stage (phase IV), discharge current remains constant at 5 A for approximately 70 µs. Discharge voltage also remains constant. This plateau of discharge current can be attributed to dCMS discharge [36]. This low level of stable discharge plateau indicates the lower plasma density in bulk volume which is due to above-mentioned reasons in phase III. However, self-sputtering process is known to generate larger amount of secondary electrons in target vicinity which in terms increase the ionization of target material sputtered atoms [36].

At last, the discharge current drops down to zero within approximately 30 µs but the discharge voltage remains constant until the discharge pulse is switched off (phase V). Effective electron temperature reaches to the minimum value and can sustained for several milliseconds after the pulse which affects the low-energy ion bombardment of growing film [49].

Temperature measured near substrate with a temperature strip was found to be approximately 200 °C. Since no intentional external heating of the substrates was performed, the increased temperature at the substrate region was due to interaction of plasma and energy flux of arriving species to the substrate [51]. This one-time deposition temperature measurement does not provide any certain quantitative value, rather provides a qualitative perception of the interaction between the energy flux and the substrate surfaces.

The deposition rate was found to be 8.16 µm/hr which is 19 times higher than that of the reported value while CN_x film depositing by Ar/N_2 reactive HiPIMS system [52]. This increase in deposition rate can be attributed to the increase in formation of C–N radicals at the target surface because of C_2H_2 gas inclusion with Ar/N_2 gaseous precursors as well as to an increase in the physical sputtering yield of the graphite target [53].

3.2 Material Characterization Results

The SEM cross-sectional micrograph of the deposited a-CN_x coating on Si substrate is presented in Fig. 5. The thickness of the coating material was found to be 400 ± 0.1 µm (the expanded uncertainty value was calculated considering the calibration uncertainty of the instrument with the coverage factor $k = 2$). Figure 5 shows the fractured columnar structures with competitive growth of different grains as well as horizontal layering microstructure. The structure can be characterized as amorphous since no particular structure such as particles, agglomerates or porous clusters are observed from SEM micrograph. Vertical cracks among the columnar structures are also visible from cross section. These cracks may originate due to high energy ion bombardment (at high impulse cathode voltage) of the growing film surface. Horizontal layering structures are formed due to interrupted deposition process. The coating deposition process was stopped after each 10 h (total deposition time was 49 h) and allowed to cool down the substrate overnight. There are five distinct horizontal layers, and each layer thickness is 80 µm (measured from SEM cross section). Higher ionization of carbon appended with low peak power and plateau discharge, the plasma density of the reactive HiPIMS described in this work is low [45]. At this low plasma density of $Ar/N_2/C_2H_2$ reactive sputtering process, competition between the incoming depositing ion flux to substrate and the surface etching of growing film cannot activate the substrate surface for the growth of densely packed columnar microstructure, which in result may form large fractured columnar structure spreading over the whole thickness of the horizontal layering structure.

Figure 6 shows the Raman spectrum of the deposited a-CN_x coating. In Raman spectra, from 1000 to 2000 cm^{-1}, microstructure of amorphous carbon film can
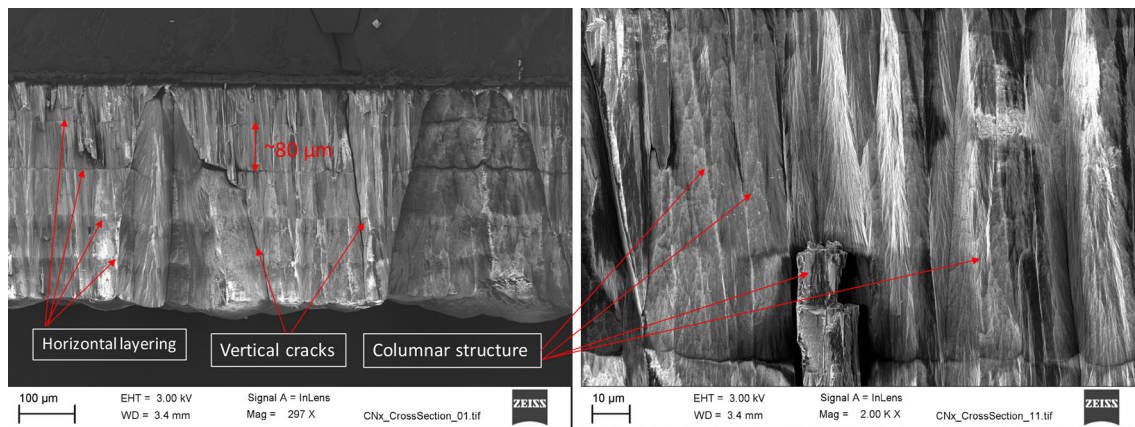
Fig. 5 SEM cross section of deposited CN_x coating material. SEM micrograph shows fractured columnar structures and horizontal layering structures. Vertical cracks are also observed in the microstructure

be characterized by two prominent features such as the position of D (disorder) peak and G (graphitic) peak as well as by the intensity ratio of these two peaks, i.e., I_D/I_G. G peak centered around 1560 cm^{-1} is attributed to the in-plane vibration of all sp^2 hybridized bonds, and D peak centered around 1350 cm^{-1} is attributed to having defect sites in sp^2 sites linking to the formation of sp^3 hybridization while I_D/I_G correlates to the sp^2 cluster fractions in organized carbon rings [54, 55]. In Fig. 6, after fitting with base line corrected Lorentzian components the observed D peak (positioned at $\sim$ 1356 cm^{-1}), G peak (positioned at $\sim$ 1565 cm^{-1}) and I_D/I_G ($\sim$ 1.3) indicate that the deposited a-CN_x coating is mainly composed of sp^2 hybridized bonds. Formation of sp^2 hybridization of carbon bonds depends on the peak discharge voltage [56]. At low discharge voltage, the incoming sputtered carbon ions or atoms do not have enough energy to form sp^3 bonds, rather graphitization occurs. However, in our case at higher peak discharge voltage ($>$ 1000 V), the high energy
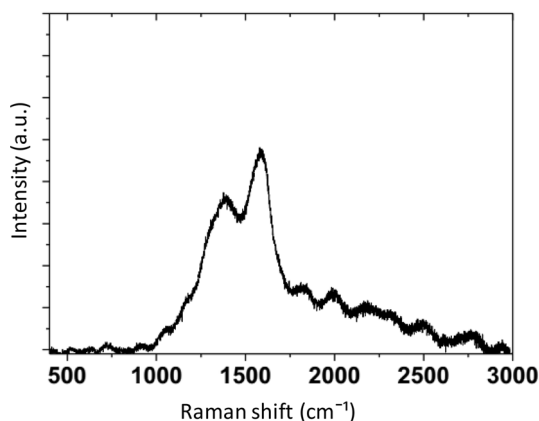
ion bombardment of the growing films damages the sp^3 sites and thus facilitates to form sp^2 hybridization through the conversion of sp^3 bonds [30, 57, 58]. Furthermore, graphitization in the a-CN_x coating can also be realized by the presence of high percentage (33.33% in partial pressure) of N_2 gas in the deposition process. At higher partial pressure of nitrogen gas chemical sputtering of growing film surface or surface etching is enhanced, which increases the probability to form volatile molecules between the nitrogen and hydrogen atoms in unstable lattice sites [59]. As a result, the disordered structure reduces the energy by relaxing some compressive stress, which eventually favor the formation of sp^2 bonds [60, 61]. Jiang et al. [62] described that above 12% nitrogen concentration more sp^2 carbon bonds are formed by preferential thermodynamic and kinetic reactions. Wang et al. [61] pointed out that sp^2 bonded carbon atoms increases with increasing nitrogen partial pressure.

AFM topography of the a-CN_x coating, shown in Fig. 7, reveals that the fractal islands of different sizes are randomly distributed on the deposited coating surface. The measured root-mean-square surface roughness value (S_q) is 0.88 ± 0.05 μm (the expanded uncertainty value was calculated based on the calibration uncertainty in Z axis measurement of the instrument, with the coverage factor $k = 2$, which is $\pm 3\%$ of 200 nm surface roughness for 10 μm Si piece). This high surface roughness value can be attributed to the formation of larger amount of sp^2 clusters [29] which is evident from the Raman spectrum of the deposited a-CN_x coating. Formation of larger amounts sp^2 clusters can be ascribed to the lower ion energy bombardment of growing film during the deposition process due to lack of externally applied substrate bias voltage. At floating bias voltage (~ -20 V) and at longer pulse width (400 μs) where the plateau discharge region is large (comparable to dcMS), the energy of incoming ions to the

Fig. 6 Raman spectra of the CN_x coating. Observed D peak is positioned around 1356 cm^{-1}, and G peak is positioned around 1565 cm^{-1}
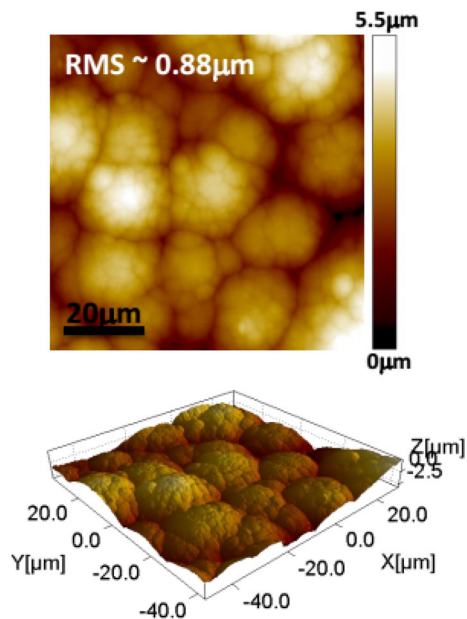
Fig. 7 AFM topography image of the a-CNx coating [13]. Higher surface roughness is due to larger amount of sp^2 clusters

substrate is not high enough to enter the sublayers of the coating material, rather those ions remain trapped onto the surface of the growing coating microstructure, which in result forms larger amount of sp^2 clusters [28]. Again, at higher pulse frequency as in this experiment (300 Hz) the frequent ion bombardment of growing coating surface elevate the surface temperature which eventually facilitates the formation of larger sp^2 clusters and coarsen the deposited coating surface [29].

EDS elemental mapping of the microstructure cross section reveals that a-CN$_X$ layer is mainly composed of 77% C, 9% N and 14% O (by mass). These percentage values of different elements are estimated average values of taken from the same cross-sectional area of Fig. 5 The presence of oxygen is due to the air exposure of the coating after the deposition process. The lower nitrogen-to-carbon ratio (N/C) in resultant a-CN$_X$ coating can be attributed to the increased re-sputtering or chemical sputtering of growing coating surface [63], due to which etching rate of N-containing species from coating surface wins over the implantation rate of energetic N species into the growing coating surface [61].

The operational temperature range test of the deposited a-CN$_X$ coating material revealed that it can withstand 400 ± 6 °C without cracking or delaminating from the substrate. The expanded uncertainty value was calculated considering only the temperature incremental step of the equipment (10 °C) with the coverage factor $k = 2$.

3.3 Mechanical Properties of the a-CN$_X$ Coating

The calculated density of the a-CN$_X$ coating was found to be 1.72 ± 0.05 gm/cm^3. The expanded uncertainty was calculated considering the width, height and thickness measurement uncertainties of the test pieces with the coverage factor $k = 2$. Weight measurement uncertainties were negligible because of low standard deviation (0.0002 gm of 10 repeated measurements) of the measurements as well as low calibration uncertainty of the weighing instrument (25% of 0.2 mg). The calculated mass density of the deposited a-CN$_X$ coating layer reveals that it has a relatively lower density comparing to that of the reported value of theoretical graphite density (2.26 g/cm^3) [40]. High energy ion bombardment with higher ion flux to the substrate leads to dense microstructure and high internal stress in carbon nitride films [63]. In the absence of applied negative bias voltage and at high process pressure ($\sim$ 3 Pa), the incoming ion flux as well as the energy of that ion flux is not high enough to remove voids or porosities entirely from microstructure [64]. This results in low mass density and low internal stress of the as-deposited thick a-CN$_X$ coating.

The measured Young's modulus and hardness of the deposited a-CN$_X$ coating by Vickers micro-indentation test is 16 ± 3 GPa and 166 ± 15 HV, respectively. The reported expanded uncertainties in Young's modulus and hardness are based on the standard deviation of the mean of 12 repeated indentation measurements with the coverage factor $k = 2$. One possible reason of this high standard deviation of the mean of Young's modulus and hardness measurement values could be the coating material is inhomogeneous in nature. Load–displacement curve of indentation test in Fig. 8 shows that 62% indentation work is due to elastic deformation indicating that the resilient or elastic recovery property of the coating material is higher than that of mild steel and gray cast iron ($\sim$ 15%) as well as it is comparable to hard rubber [12]. Such kind of resilient property indicates that when the coating material undergoes bending or compressive loading it may exhibit recoverable grain boundary sliding effect instead of plastic flow [12]. The hardness and Young's modulus of amorphous CN$_X$ film depend on the rigidity of cross-linking in various hybridized sp^3 and sp^2 carbon bonds [65]. Higher amount of sp^3 bonds and distortion in sp^2 clusters increase the degree of cross-linking in amorphous material and consequently improve mechanical properties [66, 67]. Low hardness and Young's modulus of the as-deposited a-CN$_X$ coating can be attributed to the presence of larger amount of sp^2 sites and clusters in amorphous microstructure, which was confirmed by the Raman spectroscopy and AFM analysis as described in Sect. 3.2.
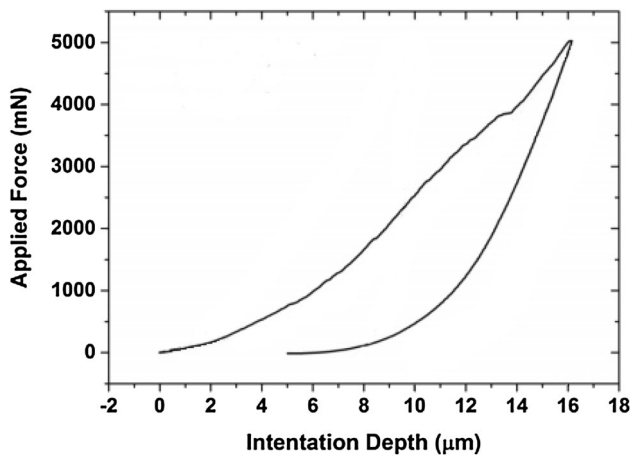
Fig. 8 Loading unloading curve of the deposited a-CNx coating material

3.4 Mechanical Damping Lossfactor Result

The damping measurement results of the uncoated and coated samples at four different force levels are summarized in Fig. 9. It is only the first bending mode's system lossfactor that is measured for uncoated and coated steel bar and material lossfactor of a-CN$_X$ coating is estimated as mentioned in Sect. 2.3. The presented a-CN$_X$ coating material was deposited on both side of the steel bar and each side coating thickness was 400 μm. Figure 9 shows that the system lossfactor value of a-CN$_X$-coated steel bar increases with increasing force level. Table 2 shows the measured system damping lossfactor values and calculated material damping lossfactor value of the investigated a-CN$_X$ coating for the first bending deformation mode at different excitation force levels.

The reported expanded uncertainties in system damping lossfactor values of uncoated and coated bar as well as in material lossfactor value of the coating in Table 2 were calculated by multiplying the standard uncertainty with a coverage factor $k = 2$. The standard uncertainty for system damping lossfactor value is the standard deviation of mean of the four repeated measurements of each sample (coated and uncoated steel bar). Other sources of measurement uncertainty have been omitted due to the facts as described in Sect. 2.3. In case of material damping lossfactor calculation, the standard uncertainty is taken from the standard deviation of mean of 59 calculated lossfactor values according to Eq. (2). The corresponding calculated loss modulus (Young's modulus multiplied by damping lossfactor) of the a-CN$_X$ coating was found to be 0.234 ± 0.011 GPa. The expanded uncertainty is calculated from the standard uncertainty of material lossfactor calculation with a coverage factor $k = 2$.

From Table 2, it can be observed that comparing to uncoated sample a-CN$_x$-coated sample has lower lossfactor value at lower level of exciting force (from force level 1 to 3) but at higher exciting force (at force level 4) the a-CN$_X$-coated steel bar has higher lossfactor value. This is due to the reason that at lower excitation force the coating has essentially lower damping property comparing to the mechanical system comprising of the steel bar and inverted shaker. Mechanical strain energy (potential energy) distribution of each vibration mode concentrates at node points of each mode and kinetic energy (maximum displacement) happens at anti-node points [68]. For a-CN$_X$-coated steel bar strain energy is mostly concentrated in the coating layer since the coated steel bar has the higher bending moment than that of uncoated steel bar. Mechanical system damping can be originated both from the strain energy due to the material's intrinsic damping and from the friction damping effect due to the stinger moves in and out of the shaker in Fig. 3. So, it can be speculated that the damping lossfactor value of the a-CN$_x$ coating material depends on excitation force level and at low level of excitation force the strain energy of the coating material is not enough to dissipate the mechanical vibrational energy.

The deposited a-CN$_X$ coating was also measured for its specific surface area and porosity, and the results showed that the BET (Brunauer–Emmett–Teller) surface area of coating is about 14.7 m^2/g, 3.4% of the volume is filled with pores, and the average pore size is around 5.8 nm. Material and structural (system) damping capacity of the deposited coating material can be realized from the frictional energy losses between the columnar structures as well as grain boundary sliding between the horizontal layers during the bending deformation at high excitation force level [69]. Under the high frequency bending deformation, voids or vertical fractures and porosities in the coating microstructure can relax the columnar structure boundaries and thus provide enough space for activating interface slippage mechanism [70]. This kind of interface slippage mechanism can enhance vibrational friction energy loss due to having larger boundary contact area and many interfaces in the columnar structures [71]. However, the boundary damping between the coating and substrate, observed by Yu et al. [72], is not observed in this work. One reason could be that the force level exerted on the specimen by the shaker is small and such nonlinear damping mechanism is not excited. Another reason could be that the adhesion between the coating and substrate is very high and vibration energy is not high enough to see any differences in strain energy distribution at the interface between the coating and substrate.

Fig. 9 System lossfactor value of the uncoated and a-CN$_X$-coated steel bar with standard deviation of mean with 95% confidence interval at four different excitation force levels
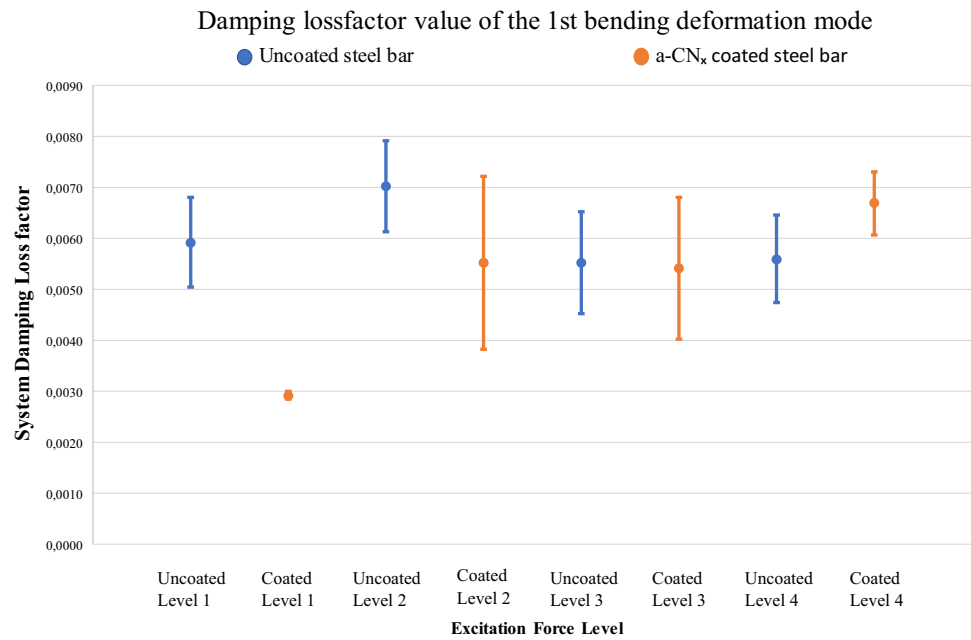

Damping lossfactor value of the 1st bending deformation mode

● Uncoated steel bar ● a-CN$_x$ coated steel bar

Table 2 First bending mode system and material damping lossfactor values at different excitation force level

Excitation Force	System damping lossfactor of uncoated steel bar	System damping lossfactor of coated steel bar	Material damping lossfactor of the a-CN$_X$ coating material
Force level 1	0.0059 ± 0.0009	0.0029 ± 0.0001	N/A
Force level 2	0.0070 ± 0.0009	0.0055 ± 0.0017	N/A
Force level 3	0.0055 ± 0.0010	0.0054 ± 0.0014	N/A
Force level 4	0.0056 ± 0.0009	0.0067 ± 0.0006	0.015 ± 0.001

4 Conclusions

A 400-µm thick amorphous CN$_X$ coating material was successfully synthesized by means of plasma-enhanced chemical vapor deposition process. For this purpose, high-power impulse magnetron sputtering of graphite target plate was used in reactive Ar/N$_2$/C$_2$H$_2$ environment.

Density of the coating material was found to be 1.72 ± 0.05 gm/cm^3 which is less than the commercial graphite's density but comparable with manufactured non-impregnated graphitic material. Microstructure characterization of the deposited a-CN$_x$ coating showed that the fractured columnar structure growth spreading over the whole thickness. Horizontal layering structure was also observed due to interrupted coating deposition process. The discharge current characteristics of the reactive HiPIMS demonstrated in this work explained that plateau discharge in longer pulse width, higher peak cathode voltage but lower peak power density as well as higher partial pressure percentage of N$_2$ and C$_2$H$_2$ precursor gases combinedly facilitate the growth of larger amount of sp^2 hybridized

carbon sites and clusters of columnar structures. EDS elemental mapping revealed that more that 70% C (by mass percentage) is present in the coating material while N content is very low (< 10%). Micro-Raman spectroscopy of the a-CN$_X$ material illustrated that the material is amorphous in nature and enriched in sp^2 hybridized carbon bonds. RMS surface roughness was found to be as high as 0.88 ± 0.05 µm. AFM topography and Raman spectra analysis suggested that larger amount of sp^2 clusters present in the material is responsible for high surface roughness.

Vickers micro-indentation test revealed that the a-CN$_X$ coating is soft in nature having lower Young's modulus and hardness value comparing to the values of CN$_X$ materials reported in various previous studies. 62% elastic recovery was observed by load–displacement curve. From previous studies, it was conformed that larger amount of sp^2 hybridized bonds, built up during the deposition process facilitated by high process pressure and floating negative bias voltage, result in low hardness and Young's modulus but high resilient (elastic recovery) property.

Furthermore, alternating hard and soft layering of coating material due to interrupted deposition process might also make the coating material soft by relaxing the intrinsic compressive stress which is induced during the competitive columnar structure growth. Though the coating material is soft in nature, it can withstand 400 ± 6 °C before delaminating from the substrate.

Mechanical damping measurement by inverted shaker test demonstrated that the deposited a-CN_X material has damping lossfactor value of 0.015 ± 0.001 at high excitation force under first bending deformation mode. From analysis, it was speculated that at high excitation force level interfacial frictional energy loss between the columnar structures as well as horizontal layering structures is the dominating factor for the enhanced damping capacity. The loss modulus (0.234 ± 0.011 GPa) of the coating material is higher than the commercial 3 M viscoelastic material (which has typical Young's modulus of 10 MPa and damping lossfactor > 0.5) which indicates that the reported a-CN_X coating can be applied to the critical mechanical components such as cutting tool shanks, shims for cutting insert, turbine blades, turbo chargers of automotive vehicles, spindles in different machine tools for suppressing vibrations.

References

1. Fanchini G, Tagliaferro A (2006) Correlation between local structure and film properties in amorphous carbon materials. In: Messina G, Santangelo S (eds) Carbon, vol 100. Topics in applied physics. Springer, Berlin Heidelberg, pp 95–105

2. Tamura N, Aono M, Harata T et al (2014) DC electrical conductivity study of amorphous carbon nitride films prepared by reactive RF magnetron sputtering. Jpn J Appl Phys 53:02BC03. https://doi.org/10.7567/jjap.53.02bc03

3. Broitman E, Neidhardt J, Hultman L (2008) Fullerene-like carbon nitride: a new carbon-based tribological coating. In: Donnet C, Erdemir A (eds) Tribology of diamond-like carbon films. Springer, Boston, pp 620–653

4. Wienss A, Persch-Schuy G, Hartmann R et al (2000) Sub-nanometer scale tribological properties of nitrogen containing carbon coatings used in magnetic storage devices. J Vac Sci Technol A Vac Surf Film 18:2023–2026. https://doi.org/10.1116/1.582466

5. Wei S, Shao T, Ding P (2011) Improvement of orthodontic friction by coating archwire with carbon nitride film. Appl Surf Sci 257:10333–10337. https://doi.org/10.1016/J.APSUSC.2011.06.055

6. Yatsuzuka M, Oka Y, Nishijima M, Hiraga K (2008) Microstructure of interface for high-adhesion DLC film on metal substrates by plasma-based ion implantation. Vacuum 83:190–197. https://doi.org/10.1016/J.VACUUM.2008.03.021

7. Field SK, Jarratt M, Teer DG (2004) Tribological properties of graphite-like and diamond-like carbon coatings. Tribol Int 37:949–956. https://doi.org/10.1016/J.TRIBOINT.2004.07.012

8. Stallard J, Mercs D, Jarratt M et al (2004) A study of the tribological behaviour of three carbon-based coatings, tested in air, water and oil environments at high loads. Surf Coat Technol 177–178:545–551. https://doi.org/10.1016/S0257-8972(03)00925-3

9. Yang S, Teer D (2000) Investigation of sputtered carbon and carbon/chromium multi-layered coatings. Surf Coat Technol 131:412–416. https://doi.org/10.1016/S0257-8972(00)00859-8

10. Sjöström H, Stafström S, Boman M, Sundgren J-E (1995) Superhard and elastic carbon nitride thin films having fullerene-like microstructure. Phys Rev Lett 75:1336–1339. https://doi.org/10.1103/PhysRevLett.75.1336

11. Fu Q, Lundin D, Nicolescu CM (2014) Anti-vibration engineering in internal turning using a carbon nanocomposite damping coating produced by PECVD process. J Mater Eng Perform 23:506–517. https://doi.org/10.1007/s11665-013-0781-y

12. Fu Q, Lorite GS, Rashid MM-U et al (2015) Suppressing tool chatter with novel multi-layered nanostructures of carbon based composite coatings. J Mater Process Technol 223:292–298. https://doi.org/10.1016/j.jmatprotec.2015.03.043

13. Fu Q, Lorite GS, Rashid MMU et al (2016) High dynamic stiffness mechanical structures with nanostructured composite coatings deposited by high power impulse magnetron sputtering. Carbon N Y 98:24–33. https://doi.org/10.1016/j.carbon.2015.10.074

14. Kleinsorge B, Ferrari AC, Robertson J et al (2000) Bonding regimes of nitrogen in amorphous carbon. Diam Relat Mater 9:643–648. https://doi.org/10.1016/S0925-9635(99)00309-X

15. Voevodin AA, Jones JG, Back TC et al (2005) Comparative study of wear-resistant DLC and fullerene-like CNx coatings produced by pulsed laser and filtered cathodic arc depositions. Surf Coat Technol 197:116–125. https://doi.org/10.1016/J.SURFCOAT.2004.06.021

16. Bakoglidis KD, Schmidt S, Garbrecht M et al (2015) Low-temperature growth of low friction wear-resistant amorphous carbon nitride thin films by mid-frequency, high power impulse, and direct current magnetron sputtering. J Vac Sci Technol A Vac Surf Film 33:05E112. https://doi.org/10.1116/1.4923275

17. Robertson J (2002) Diamond-like amorphous carbon. Mater Sci Eng R Rep 37:129–281. https://doi.org/10.1016/S0927-796X(02)00005-0

18. Logothetidis S, Charitidis C, Patsalas P (2002) Engineering properties of fully sp3- to sp2-bonded carbon films and their modifications after post-growth ion irradiation. Diam Relat Mater 11:1095–1099. https://doi.org/10.1016/S0925-9635(01)00575-1

19. Martin P, Bendavid A (2001) Review of the filtered vacuum arc process and materials deposition. Thin Solid Films 394:1–14. https://doi.org/10.1016/S0040-6090(01)01169-5

20. Voevodin AA, Donley MS (1996) Preparation of amorphous diamond-like carbon by pulsed laser deposition: a critical review.

Surf Coat Technol 82:199–213. https://doi.org/10.1016/0257-8972(95)02734-3

21. Vanhulsel A, Celis J-P, Dekempeneer E et al (1999) Inductively coupled r.f. plasma assisted chemical vapour deposition of diamond-like carbon coatings. Diam Relat Mater 8:1193–1197. https://doi.org/10.1016/S0925-9635(99)00113-2

22. Liu D, Zhang J, Liu Y et al (2005) Growth processes and surface properties of diamondlike carbon films. J Appl Phys 97:104901. https://doi.org/10.1063/1.1890446

23. Aijaz A, Sarakinos K, Raza M et al (2014) Principles for designing sputtering-based strategies for high-rate synthesis of dense and hard hydrogenated amorphous carbon thin films. Diam Relat Mater 44:117–122. https://doi.org/10.1016/j.diamond.2014.02.014

24. Hopwood J (1998) Ionized physical vapor deposition of integrated circuit interconnects. Phys Plasmas 5:1624–1631. https://doi.org/10.1063/1.872829

25. Helmersson U, Lattemann M, Bohlmark J et al (2006) Ionized physical vapor deposition (IPVD): a review of technology and applications. Thin Solid Films 513:1–24. https://doi.org/10.1016/j.tsf.2006.03.033

26. Muhl S, Me JM (1999) A review of the preparation of carbon nitride films. Diam Relat Mater 8:1809–1830. https://doi.org/10.1016/S0925-9635(99)00142-9

27. Broitman E, Czigány Z, Greczynski G et al (2010) Industrial-scale deposition of highly adherent CNx films on steel substrates. Surf Coat Technol 204:3349–3357. https://doi.org/10.1016/j.surfcoat.2010.03.038

28. Wang YY, Li H, Ji L et al (2011) Microstructure, mechanical and tribological properties of graphite-like amorphous carbon films prepared by unbalanced magnetron sputtering. Surf Coat Technol 205:3058–3065. https://doi.org/10.1016/j.surfcoat.2010.11.019

29. Wang Y, Li H, Ji L et al (2010) The effect of duty cycle on the microstructure and properties of graphite-like amorphous carbon films prepared by unbalanced magnetron sputtering. J Phys D Appl Phys 43:1–8. https://doi.org/10.1088/0022-3727/43/50/505401

30. Huang M, Zhang X, Ke P, Wang A (2013) Graphite-like carbon films by high power impulse magnetron sputtering. Appl Surf Sci 283:321–326. https://doi.org/10.1016/j.apsusc.2013.06.109

31. Liao JX, Liu WM, Xu T, Xue QJ (2004) Characteristics of carbon films prepared by plasma-based ion implantation. Carbon N Y 42:387–393. https://doi.org/10.1016/J.CARBON.2003.11.013

32. Broitman E, Zheng WT, Sjöström H et al (1998) Stress development during deposition of CNx thin films. Appl Phys Lett 72:2532–2534. https://doi.org/10.1063/1.121410

33. Benedikt J (2010) Plasma-chemical reactions: low pressure acetylene plasmas. J Phys D Appl Phys 43:43001. https://doi.org/10.1088/0022-3727/43/4/043001

34. Gudmundsson JT (2016) On reactive high power impulse magnetron sputtering. Plasma Phys Control Fusion 58:14002. https://doi.org/10.1088/0741-3335/58/1/014002

35. Martinu L, Zabeida O, Klemberg-Sapieha JE (2010) Plasma-enhanced chemical vapor deposition of functional coatings. In: Martin PM (ed) Handbook of deposition technologies for films and coatings. Elsevier, Amsterdam, pp 392–465

36. Gudmundsson JT, Brenning N, Lundin D, Helmersson U (2012) High power impulse magnetron sputtering discharge. J Vac Sci Technol A Vac Surf Film 30:30801. https://doi.org/10.1116/1.3691832

37. Lundin D, Sarakinos K (2012) An introduction to thin film processing using high-power impulse magnetron sputtering. J Mater Res 27:780–792. https://doi.org/10.1557/jmr.2012.8

38. Kouznetsov V, Nicolescu M, Meza O, Hemmingsson L (2008) Method, material and apparatus for enhancing dynamic stiffness. WO application patent. WO2008105736(A2)

39. Chen C-C, Hong FC-N (2005) Structure and properties of diamond-like carbon nanocomposite films containing copper nanoparticles. Appl Surf Sci 242:261–269. https://doi.org/10.1016/J.APSUSC.2004.08.036

40. Oliver WC, Pharr GM (2004) Measurement of hardness and elastic modulus by instrumented indentation: advances in understanding and refinements to methodology. J Mater Res 19:3–20. https://doi.org/10.1557/jmr.2004.19.1.3

41. Malogi D, Gupta A, Kathawate GR (2009) Center impedance method for damping measurement. Adv Acoust Vib 2009:1–7. https://doi.org/10.1155/2009/319538

42. Barkanov E, Gassan J (1995) Frequency response analysis of laminated composite beams. Mech Compos Mater 30:484–492. https://doi.org/10.1007/BF00616777

43. Torvik PJ (2007) Analysis of free-layer damping coatings. Key Eng Mater 333:195–214. https://doi.org/10.4028/www.scientific.net/KEM.333.195

44. Aiempanakit M, Aijaz A, Lundin D et al (2013) Understanding the discharge current behavior in reactive high power impulse magnetron sputtering of oxides. J Appl Phys 113:133302. https://doi.org/10.1063/1.4799199

45. Anders A, Andersson J, Ehiasarian A (2007) High power impulse magnetron sputtering: current-voltage-time characteristics indicate the onset of sustained self-sputtering. J Appl Phys 102:133303. https://doi.org/10.1063/1.2817812

46. Magnus F, Sveinsson OB, Olafsson S, Gudmundsson JT (2011) Current-voltage-time characteristics of the reactive Ar/N2 high power impulse magnetron sputtering discharge. J Appl Phys 110:083306. https://doi.org/10.1063/1.3653233

47. Čapek J, Hála M, Zabeida O et al (2012) Steady state discharge optimization in high-power impulse magnetron sputtering through the control of the magnetic field. J Appl Phys 111:023301. https://doi.org/10.1063/1.3673871

48. Vitelaru C, Lundin D, Stancu GD et al (2012) Argon metastables in HiPIMS: time-resolved tunable diode-laser diagnostics. Plasma Sources Sci Technol 21:25010. https://doi.org/10.1088/0963-0252/21/2/025010

49. Poolcharuansin P, Bradley JW (2010) Short- and long-term plasma phenomena in a HiPIMS discharge. Plasma Sources Sci Technol 19:25010. https://doi.org/10.1088/0963-0252/19/2/025010

50. Lundin D, Al Sahab S, Brenning N et al (2011) Internal current measurements in high power impulse magnetron sputtering. Plasma Sources Sci Technol 20:45003. https://doi.org/10.1088/0963-0252/20/4/045003

51. Kouznetsov V, Macák K, Schneider JM et al (1999) A novel pulsed magnetron sputter technique utilizing very high target power densities. Surf Coat Technol 122:290–293. https://doi.org/10.1016/S0257-8972(99)00292-3

52. Kimura T, Nishimura R (2015) Formation of amorphous carbon nitride films by reactive Ar/N2 high-power impulse magnetron sputtering. Jpn J Appl Phys 6:1–7. https://doi.org/10.7567/JJAP.54.01AD06

53. Shi JR (2006) Study on nitrogenated amorphous carbon films prepared by unbalanced magnetron sputtering. J Appl Phys 99:033505. https://doi.org/10.1063/1.2168027

54. Ferrari AC, Robertson J (2001) Resonant Raman spectroscopy of disordered, amorphous, and diamondlike carbon. Phys Rev B 64:75414. https://doi.org/10.1103/PhysRevB.64.075414

55. Dwivedi N, Rismani-Yazdi E, Yeo RJ et al (2015) Probing the role of an atomically thin SiNx interlayer on the structure of ultrathin carbon films. Sci Rep 4:5021

56. Horwat D, Anders A (2010) Compression and strong rarefaction in high power impulse magnetron sputtering discharges. J Appl Phys 108:123306. https://doi.org/10.1063/1.3525986

57. Robertson J (2002) Diamond-like amorphous carbon. Mater Sci Eng R Rep 37:129–281. https://doi.org/10.1016/S0927-796X(02)00005-0

58. Liu E, Li L, Blanpain B, Celis JP (2005) Residual stresses of diamond and diamondlike carbon films. J Appl Phys 98:73515. https://doi.org/10.1063/1.2071451

59. Hellgren N, Macák K, Broitman E et al (2000) Influence of plasma parameters on the growth and properties of magnetron sputtered CNx thin films. J Appl Phys 88:524. https://doi.org/10.1063/1.373690

60. McKenzie DR, Muller D, Pailthorpe BA (1991) Compressive-stress-induced formation of thin-film tetrahedral amorphous carbon. Phys Rev Lett 67:773–776. https://doi.org/10.1103/PhysRevLett.67.773

61. Wang XC, Wu P, Li ZQ et al (2004) Microstructure of amorphous carbon nitride films fabricated by facing-target reactive magnetron sputtering. J Phys D Appl Phys 37:2127–2134. https://doi.org/10.1088/0022-3727/37/15/012

62. Hu J, Yang P, Lieber CM (1998) Nitrogen-driven sp3 to sp2 transformation in carbon nitride materials. Phys Rev B 57:R3185–R3188. https://doi.org/10.1103/PhysRevB.57.R3185

63. Chan W, Zhou B, Chung Y et al (1998) Synthesis, composition, surface roughness and mechanical properties of thin nitrogenated carbon films. J Vac Sci Technol A Vac Surf Film 16:1907–1911. https://doi.org/10.1116/1.581194

64. Li D, Chung Y-W, Wong M-S, Sproul WD (1995) Mechanical properties of amorphous carbon nitride thin films prepared by reactive magnetron sputter-deposition. Tribol Lett 1:87–93. https://doi.org/10.1007/BF00157978

65. Baptista DL, Zawislak FC (2004) Hard and sp2-rich amorphous carbon structure formed by ion beam irradiation of fullerene, a-C and polymeric a-C: H films. Diam Relat Mater 13:1791–1801. https://doi.org/10.1016/J.DIAMOND.2004.04.006

66. Lee K-R, Kim M-G, Cho S-J et al (1997) Structural dependence of mechanical properties of Si incorporated diamond-like carbon films deposited by RF plasma-assisted chemical vapour deposition. Thin Solid Films 308–309:263–267. https://doi.org/10.1016/S0040-6090(97)00411-2

67. Kim T-Y, Lee CS, Lee YJ et al (2007) Reduction of the residual compressive stress of tetrahedral amorphous carbon film by Ar background gas during the filtered vacuum arc process. J Appl Phys 101:23504. https://doi.org/10.1063/1.2408385

68. Beranek LL, Ver IL (1992) Noise and vibration control engineering—principles and applications. Wiley, New York

69. Koratkar N, Wei BQ, Ajayan PM (2002) Carbon nanotube films for damping applications. Adv Mater 14:997–1000

70. Yu L, Ma Y, Zhou C, Xu H (2005) Damping capacity and dynamic mechanical characteristics of the plasma-sprayed coatings. Mater Sci Eng A 407:174–179. https://doi.org/10.1016/J.MSEA.2005.07.051

71. Suhr J, Koratkar NA, Ye D, Lu T-M (2006) Damping properties of epoxy films with nanoscale fillers. J Intell Mater Syst Struct 17:255–260. https://doi.org/10.1177/1045389X06055295

72. Yu L, Ma Y, Zhou C, Xu H (2005) Damping efficiency of the coating structure. Int J Solids Struct 42:3045–3058. https://doi.org/10.1016/J.IJSOLSTR.2004.10.033